

Eight-dimensional topological systems simulated using time-space crystalline structures

Yakov Braver,¹ Egidijus Anisimovas,¹ and Krzysztof Sacha²

¹*Institute of Theoretical Physics and Astronomy,
Vilnius University, Saulėtekio 3, LT-10257 Vilnius, Lithuania*

²*Instytut Fizyki Teoretycznej, Uniwersytet Jagielloński,
ulica Profesora Stanisława Łojasiewicza 11, PL-30-348 Kraków, Poland*

We demonstrate the possibility of using time-space crystalline structures to simulate eight-dimensional systems based on only two physical dimensions. A suitable choice of system parameters allows us to obtain a gapped energy spectrum, making topological effects become relevant. The nontrivial topology of the system is evinced by considering the adiabatic state pumping along temporal and spatial crystalline directions. Analysis of the system is facilitated by rewriting the system Hamiltonian in a tight-binding form, thereby putting space, time, and the additional synthetic dimensions on an equal footing.

Introduction. Quantum simulation is a rapidly growing and exciting field of study, focused on exploiting controllable quantum systems to replicate and probe complex physical phenomena [1, 2]. Whereas simulating a quantum system with full precision is a daunting task, recreation of specific relevant features is often within reach. In particular, ultracold atomic systems in optical lattices [3] have successfully demonstrated abilities to model intricate condensed-matter and topological phenomena [4, 5] as well as lattice gauge theories [6, 7]. An intriguing line of thought along this direction is the emulation of high-dimensional systems, notably — high-dimensional periodically ordered physical structures — in low-dimensional settings [5, 8–12]. In this context, several recent proposals drew inspiration from the emergent concept of time crystals [13–16] and asked if time can play the role of an additional coordinate in quantum simulations. This time-crystalline approach [16, 17] involves a driving signal of a certain frequency to create a repeating pattern of motion at a commensurate frequency that persists over time. Many condensed matter phenomena were thus reenacted in the time domain [16, 18], and the possibility to engage both temporal and spatial dimensions at the same time was established [11, 19–21], thus doubling the number of available dimensions.

In this Letter, we provide a route for studying topological eight-dimensional (8D) systems that can be experimentally realized using only two physical spatial dimensions. We start with a periodically driven 1D optical lattice with steep barriers (modeled by delta-functions) and show that it can sustain a 2D time-space lattice. The topological nature of the attained time-space crystalline structure is made evident by considering adiabatic state pumping along temporal and spatial crystalline directions. Interpreting the two adiabatic phases as crystal momenta of simulated extra dimensions, we show that the energy bands of the system are characterized by non-vanishing second Chern numbers of the effective 4D lattice. Finally, we demonstrate that two such 4D systems

can be combined, and the resulting energy spectrum will remain gapped. The topological properties of the attained 8D system are then characterized by the fourth Chern number, and energy bands with nonvanishing values of the fourth Chern number are identified.

Model. We introduce a 1D time-dependent Hamiltonian

$$\hat{H}(x, \hat{p}_x, t | \varphi_x, \varphi_t) = \hat{h}(x, \hat{p}_x | \varphi_x) + \xi(x, t | \varphi_t), \quad (1)$$

written as a sum of an adiabatic-pumping part \hat{h} (which is static but depends on a spatial adiabatic phase φ_x) and a time-periodic driving term featuring a second adiabatic phase φ_t . Throughout this work, we use the recoil units for the energy $\hbar^2 k_L^2 / 2m$ and length $1/k_L$, with k_L being the wave number of the primary laser beam used to create the optical lattice and m the particle mass. The unit of time is \hbar divided by the energy unit. The first term of Eq. (1) is the unperturbed spatial Hamiltonian,

$$\hat{h} = \hat{p}_x^2 + V \sum_{n=0}^{3N} \delta(x - \frac{na}{3}) + U \sum_{n=1}^3 g_n(x) \cos\left[\varphi_x + \frac{2\pi(n-1)}{3}\right]. \quad (2)$$

Here, \hat{p}_x is the momentum operator, while the sums describe the spatial potential — a lattice of N identical cells of length a , each consisting of three sites separated by steep delta-function barriers, see Fig. 1. The superlattice potential $g_n(x)$ is equal to unity only in the n th site of each spatial cell and vanishes otherwise. This term modulates the onsite energies in the same way in each cell by changing φ_x , with U controlling the modulation amplitude. Note that the modulation phase in each consecutive site is lagging with respect to its neighbor on the left by one third of a cycle. If the modulation is performed adiabatically, the Thouless pumping can be realized in the system described by \hat{h} . The realization of sharp optical barriers as well as three-site Thouless pumping have already been studied in the literature [22–24].

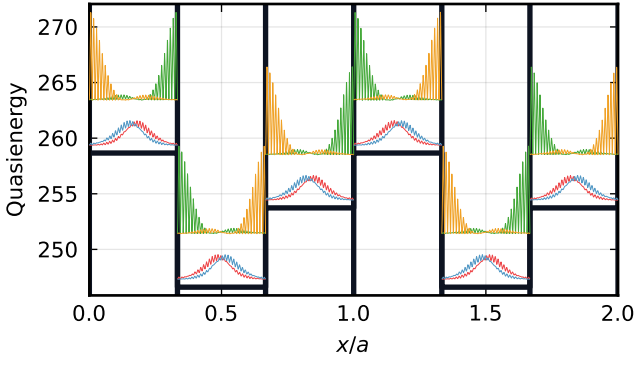


Figure 1. Wannier function densities $|w_\ell(x, t = 7\pi/4\Omega)|^2$ at $\varphi_x = \pi/5$, $\varphi_t = 0$, where $2\pi/\Omega$ is the period of time evolution of $w_\ell(x, t)$. The baseline of each Wannier function is shifted upwards along the quasienergy axis by the mean value of quasienergy in the corresponding state, i.e. the quantity $\langle w_\ell | \hat{H} | w_\ell \rangle$. At the chosen value of φ_x , each Wannier function is localized almost entirely within a single site, therefore, the infinitesimal “tails” of the functions are not shown. Black vertical lines represent the steep barriers separating the sites of the spatial lattice, while the horizontal lines depict the values of the onsite energies described by the third term in Eq. (2). Parameters of the model are: $N = 2$, $s = 2$, $a = 4.000$, $V = 2000$, $U = 7.000$, $\omega = 676.8$, $\lambda_S = 10.00$, $\lambda_L = 20.00$. Trailing zeros are within the numerical resolution/accuracy and are significant. The nature of the presented results, however, will not change if all the values are chosen within $\sim 10\%$ of the given ones and then ω is adjusted accordingly to ensure that the quasienergy spectrum is gapped.

The spatial Hamiltonian is perturbed by the terms

$$\begin{aligned} \xi(x, t | \varphi_t) = & \lambda_S \cos\left(\frac{12\pi x}{a}\right) \cos(2\omega t) \\ & + \lambda_L \cos\left(\frac{6\pi x}{a}\right) \cos(\omega t + \varphi_t), \end{aligned} \quad (3)$$

where λ_S and λ_L control the overall strength of the perturbation. The spatial frequencies $6\pi/a$ and $12\pi/a$ ensure that all spatial sites are perturbed in the same way. The driving frequency ω is chosen so that a resonant condition is fulfilled in each spatial site. In the classical description, the resonance means that ω is very close to an integer multiple of the frequency Ω of the periodic motion of a particle in a spatial site, i.e., $\omega \approx s\Omega$, where s is integer. In the quantum description, the resonance corresponds to ω being close to an integer multiple of the gap Ω between certain bands of the Hamiltonian (2). In the limit $V \rightarrow \infty$ [see Eq. (2)] an independent time-crystalline structure is formed in each spatial site due to the resonant driving. Specifically, in the frame evolving along the resonant trajectory, the resonant dynamics of a particle can be described by $\hat{H}_{\text{eff}} = \hat{p}_{\tilde{x}}^2 + \lambda_S \cos(2s\tilde{x}) + \lambda_L \cos(s\tilde{x} + \varphi_t)$ where $\tilde{x} \in [0, 2\pi)$, see Refs. [11, 21]. For example, for $s = 2$, there are two temporal cells, each consisting of two temporal sites. An adiabatic change of the phase φ_t allows for a realization of the Thouless pumping in the time-crystalline structures

[21]. If $V < \infty$, then tunneling of a particle between spatial sites is possible, and the entire system forms a 2D time-space crystalline structure which, as we will show, can be described by a 2D tight-binding model.

To study the emergence of a time-space crystalline structure and the pumping dynamics, we solve the eigenvalue problem $\hat{H}u_{n,k}(x, t) = \varepsilon_{n,k}u_{n,k}(x, t)$ for the Floquet Hamiltonian $\hat{\mathcal{H}} = \hat{H} - i\partial_t$ [25–27]. We assume periodic boundary conditions for the spatial system and introduce the spatial quasimomentum k . We denote the quasienergy of the n th eigenstate by $\varepsilon_{n,k}$, while $u_{n,k}(x, t)$ is the corresponding Floquet mode that respects temporal periodicity of the perturbation: $u_{n,k}(x, t) = u_{n,k}(x, t + 2\pi/\omega)$. A general solution of the Schrödinger equation can be represented as a superposition of states $\Psi_{n,k}(x, t) = e^{-i\varepsilon_{n,k}t}u_{n,k}(x, t)$. In our simulations we consider a finite number of spatial cells, $N = 2$, and a finite number of temporal cells, $s = 2$. The considered values of quasimomentum are thus $k = 0$ and $k = \pi$ (assuming $k \in [0; 2\pi)$), corresponding to the boundary of the Brillouin zone. Consequently, the obtained widths of the energy bands coincide with the widths being approached in the limit $N \rightarrow \infty$.

The details of the diagonalization procedure are covered in the Supplemental Material [28]. All calculations have been performed using a number of software packages [29–34] written in the Julia programming language [35]. The source code of our package is available on GitHub [36].

The resonant subspace of the entire Hilbert space which we are interested in consists of $3N \times 2s$ eigenstates. Diagonalizing the periodic position operator $e^{i\frac{2\pi}{Na}x}$ in this subspace [37, 38] we obtain $6Ns$ Wannier functions $w_\ell(x, t)$ of the $3N \times 2s$ time-space crystalline structure which are represented by localized wave packets propagating with the period $2\pi/\Omega$ along the resonant orbits in each spatial site. These Wannier functions are shown at $t = 7\pi/4\Omega$ in Fig. 1, where each spatial site hosts $2s = 4$ states.

The tight-binding picture. In the basis of the Wannier functions, the Floquet Hamiltonian restricted to the resonant subspace takes the form of the tight-binding model

$$\hat{\mathcal{H}}_{\text{TB}}(\varphi_x, \varphi_t) = \sum_{\ell', \ell} J_{\ell'\ell}(\varphi_x, \varphi_t) \hat{a}_{\ell'}^\dagger \hat{a}_\ell, \quad (4)$$

where operator \hat{a}_i^\dagger creates (while \hat{a}_i annihilates) a boson on site ℓ . Here, $\ell \in [1, 6Ns]$ enumerates all sites of the 2D time-space lattice, and it is related to the space-time index pair (j, α) as $\ell = 2s(j - 1) + \alpha$, where $j \in [1, 3N]$ and $\alpha \in [1, 2s]$. The matrix elements $J_{\ell'\ell}$ are calculated as

$$J_{\ell'\ell} = \int_0^{sT} \frac{dt}{sT} \langle w_{\ell'} | \hat{\mathcal{H}} | w_\ell \rangle, \quad (5)$$

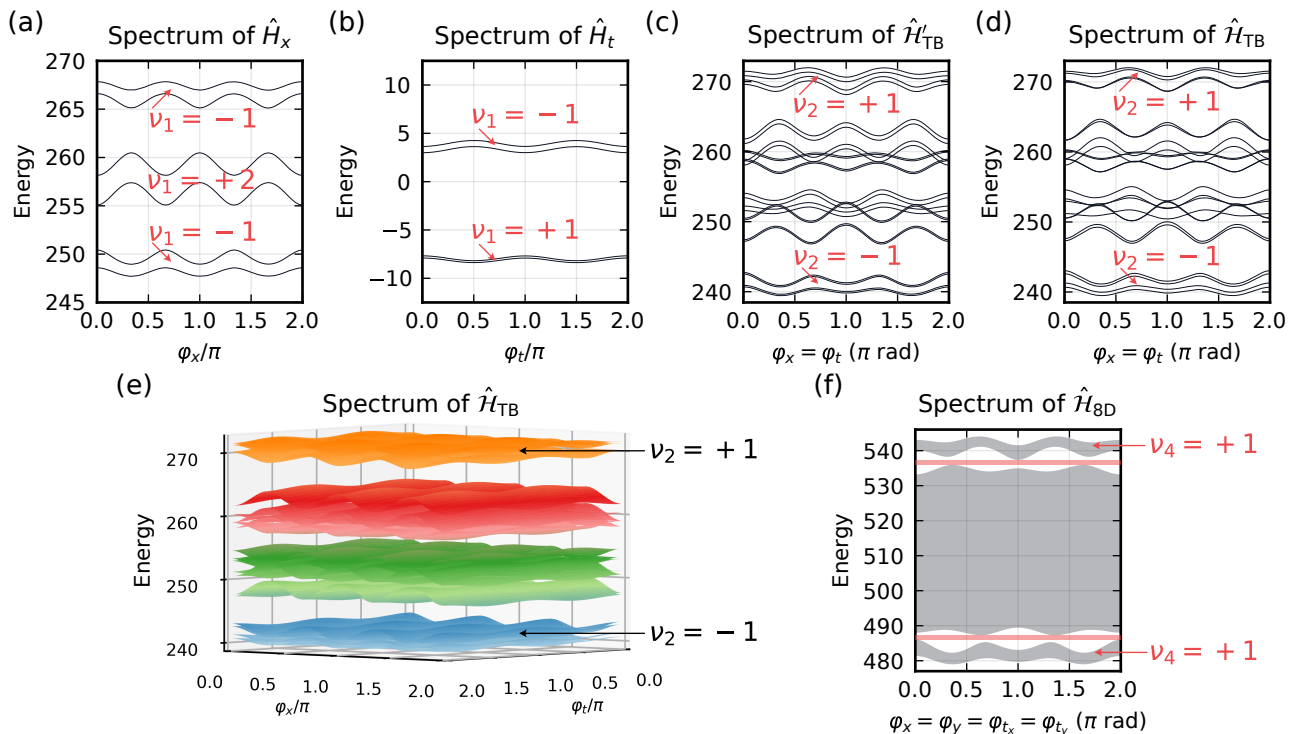


Figure 2. The energy spectra of derived systems. (a) Energy spectrum of the decomposed spatial Hamiltonian \hat{H}_x . (b) Energy spectrum of the decomposed temporal Hamiltonian \hat{H}_t . (c) Energy spectrum of \hat{H}'_{TB} , equal to the Minkowski sum of the spectra in (a) and (b). A cut of the spectrum along the line $\varphi_x = \varphi_t$ is shown. (d) Energy spectrum of \hat{H}_{TB} along the line $\varphi_x = \varphi_t$. (e) Eigenenergy surfaces of \hat{H}_{TB} . (f) Energy spectrum of an 8D systems obtained by combining two independent copies of the 4D systems whose spectra are shown in (e). The gray areas represent the bands, with individual levels not shown for visual clarity. The red regions indicate the gaps.

where $T = 2\pi/\omega$ is the driving period. The Wannier basis is constructed repeatedly for every phase φ_x and φ_t . Each state $|w_\ell(t)\rangle$ is confined to a single spatial site, consequently, only nearest-neighbor spatial couplings are relevant. Moreover, this coupling is appreciable only at times when a given state $|w_\ell(t)\rangle$ is localized near a classical turning point (see the green and yellow states in Fig. 1). At these times, each of these states has only one partner which it is coupled to. Therefore, each Wannier state is coupled to only a single state of those in the neighboring spatial sites. Provided these partners (see like-colored states in Fig. 1) are numbered with the same temporal index α , it will not change when a state transitions to a neighboring site (only j will change). This leads to a separable structure of the resulting time-space lattice, where “diagonal” transitions — those which require both indices j and α to change simultaneously — are forbidden. This is an idealized picture, but one which holds with high accuracy since next-nearest-neighbor couplings are negligible (see [28]). Note that this separability is intrinsic to the model described by Eqs. (1)–(3) and cannot be changed by tuning the parameters.

Thus, the Hamiltonian \hat{H}_{TB} is separable in the sense

that

$$\hat{H}_{\text{TB}} \approx \hat{I}_x \otimes \hat{H}_t + \hat{H}_x \otimes \hat{I}_t \equiv \hat{H}'_{\text{TB}}, \quad (6)$$

where “ \otimes ” denotes the tensor product, \hat{H}_x and \hat{H}_t are, respectively, the separated spatial and temporal Hamiltonians, while \hat{I}_x and \hat{I}_t are the identity operators acting in the spaces of, respectively, operators \hat{H}_x and \hat{H}_t . Consequently, the eigenvalue spectrum of \hat{H}'_{TB} is the Minkowski sum of eigenvalue spectra of \hat{H}_x and \hat{H}_t . We will refer to the eigenvalues of all tight-binding Hamiltonians as simply “energies”.

The spectra of \hat{H}_x and \hat{H}_t are shown in Figs. 2(a) and 2(b) together with the first Chern numbers of each band. Considering the spatial part described by \hat{H}_x , we treat the phase φ_x as a fictitious quasimomentum, allowing us to introduce the Berry curvature of the n th band, $\Omega_{k_x \varphi_x} = -2\Im \langle \partial_{k_x} \chi_{n, k_x} | \partial_{\varphi_x} \chi_{n, k_x} \rangle$, and the corresponding first Chern number [8, 39–41]

$$\nu_1^{(x)} = \frac{1}{2\pi} \int_{\text{BZ}} dk_x \int_0^{2\pi} d\varphi_x \Omega_{k_x \varphi_x}. \quad (7)$$

In the definition of the Berry curvature, $|\chi_{n, k_x}\rangle$ is the cell-periodic part of the Bloch eigenstate $e^{ik_x j} \chi_{n, k_x}(j)$ of

\hat{H}_x with $\chi_{n,k_x}(j+3) = \chi_{n,k_x}(j)$ where j labels spatial sites. For clarity, we suppress indication of the parametric dependence on φ_x in \hat{H}_x and its eigenstates. The crystal momentum k_x is treated as a continuous quantity assuming $N \rightarrow \infty$. The values of $\nu_1^{(x)}$ for the bands shown in Fig. 2(a) may be easily determined as the number of particles of a given band pumped through an arbitrary lattice cross section per pumping cycle (see [28]) or, equivalently, by counting the number of edge state branches in the spectrum of the corresponding non-periodic system [38]. In complete analogy, we introduce the time-quasimomentum k_t for the Hamiltonian \hat{H}_t , so that the eigenstates of \hat{H}_t are given by $e^{ik_t\alpha}\tau_{n,k_t}(\alpha)$ with $\tau_{n,k_t}(\alpha+2) = \tau_{n,k_t}(\alpha)$. The first Chern numbers $\nu_1^{(t)}$ of the two bands in Fig. 2(b) are then calculated by integrating the Berry curvature $\Omega_{k_t\varphi_t}$. Note that by interpreting the phases φ_x and φ_t as quasimomenta, we increase the dimensionality of the systems. Each of the Hamiltonians \hat{H}_x and \hat{H}_t thus describes a 2D system, while their combination, $\hat{\mathcal{H}}'_{\text{TB}}$, whose spectrum is shown in Fig. 2(c), describes a 4D system. The lowest and the highest bands are nondegenerate and are characterized by the second Chern numbers calculated from the Abelian Berry curvature [8, 9]. Formally, we gather the system parameters into a vector $\mathbf{R} = (k_x, \varphi_x, k_t, \varphi_t)$ and calculate the curvature as $\Omega_{\mu\nu}(\mathbf{R}) = -2\Im \langle \partial_\mu \xi_{n,k_x,k_t} | \partial_\nu \xi_{n,k_x,k_t} \rangle$ where $\partial_\mu \equiv \frac{\partial}{\partial R^\mu}$, $\mu = 1, 2, 3, 4$, and $|\xi_{n,k_x,k_t}\rangle$ is the cell-periodic part of the n th band eigenstate of $\hat{\mathcal{H}}'_{\text{TB}}$. Due to the factorization $|\xi_{n,k_x,k_t}\rangle = |\chi_{n,k_x}\rangle \otimes |\tau_{n,k_t}\rangle$, the general formula for the second Chern number [8, 9] reduces to

$$\nu_2^{(x,t)} = \frac{1}{4\pi^2} \int d^4R \Omega_{k_x\varphi_x} \Omega_{k_t\varphi_t} = \nu_1^{(x)} \nu_1^{(t)}. \quad (8)$$

The values of $\nu_2^{(x,t)}$ are indicated in Fig. 2(c).

Comparing the spectrum of $\hat{\mathcal{H}}'_{\text{TB}}$ to the spectrum of the exact tight-binding Hamiltonian $\hat{\mathcal{H}}_{\text{TB}}$, shown in Fig. 2(d), we note that they are nearly identical. Slight discrepancies are to be expected since in order to obtain the separable Hamiltonian we have neglected some very weak couplings in $\hat{\mathcal{H}}_{\text{TB}}$ [28]. Nevertheless, the second Chern numbers of the bands of energy spectra of $\hat{\mathcal{H}}_{\text{TB}}$ and $\hat{\mathcal{H}}'_{\text{TB}}$ are the same. This is supported by the fact that the energy spectrum of $\hat{\mathcal{H}}_{\text{TB}}$ can be obtained by adiabatically deforming the spectrum of $\hat{\mathcal{H}}'_{\text{TB}}$ without closing the gaps in process. Relatedly, we remark that the gap below the highest resonant energy band of $\hat{\mathcal{H}}_{\text{TB}}$ remains open for all values of φ_x and φ_t , as shown in Fig. 2(e). The same is true for the gap above the lowest band of $\hat{\mathcal{H}}_{\text{TB}}$.

Higher-dimensional extensions. Finally, let us consider an optical lattice of two orthogonal spatial dimensions, so that the full system Hamiltonian $\hat{H}_{4\text{D}} = \hat{H}(x, \hat{p}_x, t | \varphi_x, \varphi_{t_x}) + \hat{H}(y, \hat{p}_y, t | \varphi_y, \varphi_{t_y})$. This produces a 4D time-space crystalline structure since the total Wannier functions now have four independent in-

degrees: $W_{\mathbf{j},\alpha}(x, y, t) = w_{j_x, \alpha_x}(x, t) w_{j_y, \alpha_y}(y, t)$, where $\mathbf{j} = (j_x, j_y)$ and $\alpha = (\alpha_x, \alpha_y)$ [11]. A two-dimensional temporal structure of $2s \times 2s$ sites now emerges in each two-dimensional spatial cell; motion in the former is characterized by the temporal quasimomenta k_{t_x} and k_{t_y} . The energy spectrum of this system may be readily obtained as a Minkowski sum of two copies of spectra in Fig. 2(e). The result is shown in Fig. 2(f), where it is apparent that the highest and the lowest bands are separated from others by a gap. This holds true not only for the displayed cut of the spectrum at $\varphi_x = \varphi_y = \varphi_{t_x} = \varphi_{t_y}$, but rather for all values of the phases. The ratio of the bandwidth of the highest band to the gap below it is found to be 5%, while the ratio of the bandwidth of the lowest band to the gap above it is 2%.

The system whose spectrum is shown in Fig. 2(f) may thus be described by a lattice Hamiltonian

$$\hat{\mathcal{H}}_{8\text{D}} = \hat{I} \otimes \hat{\mathcal{H}}_{\text{TB}}^{(x)} + \hat{\mathcal{H}}_{\text{TB}}^{(y)} \otimes \hat{I}, \quad (9)$$

where \hat{I} is an identity matrix of the same size as $\hat{\mathcal{H}}_{\text{TB}}$. The system parameters are the two crystal momenta k_x, k_y , the spatial phases φ_x and φ_y , and the four respective parameters of the two underlying temporal systems: $k_{t_x}, k_{t_y}, \varphi_{t_x}, \varphi_{t_y}$. As in the 4D case, the lowest and the highest energy bands are nondegenerate, and therefore may be characterized by the fourth Chern number of a corresponding Abelian gauge field. Generalizing (8) and related equations to 8D in a straightforward way (see [8] and [28] for details), the relevant Chern number results as $\nu_4^{(x,t_x,y,t_y)} = \nu_2^{(x,t_x)} \nu_2^{(y,t_y)}$. This way we confirm that the highest and the lowest bands in Fig. 2(f) are characterized by nonzero fourth Chern numbers, implying the topologically nontrivial nature of the system. We note that if $\hat{\mathcal{H}}_{8\text{D}}$ is constructed using two copies of the approximate Hamiltonian $\hat{\mathcal{H}}'_{\text{TB}}$, the higher gap closes, whereas the lower one remains open.

It is apparent in Fig. 2(f) that the highest and the lowest bands are wider than the gaps, implying that the gaps disappear if one more copy of the spectrum in Fig. 2(e) is added. Nevertheless, a time-space structure based on a different spatial system than the one given in (2) may exhibit even wider gaps compared to those in Fig. 2(e). This would allow one to realize a 12D time-space structure by combining three copies of $\hat{\mathcal{H}}_{\text{TB}}$, each based on a separate physical dimension (x, y , and z).

Conclusions. Summarizing, we have shown that the time-space crystals may be used as a platform for studying 8D systems that can be defined in a tight-binding form. We have devised a concrete, experimentally realizable driven quantum system with validated parameters that is an example of a topologically nontrivial 8D system. Remarkably, it is possible to realize systems with nontrivial topological properties and study the resulting effects in eight dimensions with the help of a properly driven 2D system and without involving any internal

degrees of freedom of the particles. High-dimensional spatio-temporal crystalline structures open up possibilities for building practical devices that would be unthinkable in three dimensions. The results presented in this Letter pave the way towards further research in this direction.

This research was funded by the National Science Centre, Poland, Project No. 2021/42/A/ST2/00017 (K. S.) and the Lithuanian Research Council, Lithuania, Project No. S-LL-21-3. For the purpose of Open Access, the authors have applied a CC-BY public copyright license to any Author Accepted Manuscript (AAM) version arising from this submission.

-
- [1] R. P. Feynman, Simulating physics with computers, *Int. J. Theor. Phys.* **21**, 467 (1982).
- [2] J. Fraxanet, T. Salamon, and M. Lewenstein, *The coming decades of quantum simulation* (2022), [arXiv:2204.08905](https://arxiv.org/abs/2204.08905).
- [3] F. Schäfer, T. Fukuhara, S. Sugawa, Y. Takasu, and Y. Takahashi, Tools for quantum simulation with ultracold atoms in optical lattices, *Nat. Rev. Phys.* **2**, 411 (2020), [arXiv:2006.06120](https://arxiv.org/abs/2006.06120).
- [4] C. S. Chiu, G. Ji, A. Bohrdt, M. Xu, M. Knap, E. Demler, F. Grusdt, M. Greiner, and D. Greif, String patterns in the doped Hubbard model, *Science* **365**, 251 (2019), [arXiv:1810.03584](https://arxiv.org/abs/1810.03584).
- [5] T. Ozawa and H. M. Price, Topological quantum matter in synthetic dimensions, *Nat. Rev. Phys.* **1**, 349 (2019), [arXiv:1910.00376](https://arxiv.org/abs/1910.00376).
- [6] M. C. Bañuls, R. Blatt, J. Catani, A. Celi, J. I. Cirac, M. Dalmonte, L. Fallani, K. Jansen, M. Lewenstein, S. Montangero, C. A. Muschik, B. Reznik, E. Rico, L. Tagliacozzo, K. V. Acoleyen, F. Verstraete, U.-J. Wiese, M. Wingate, J. Zakrzewski, and P. Zoller, Simulating lattice gauge theories within quantum technologies, *Eur. Phys. J. D* **74**, 165 (2020), [arXiv:1911.00003](https://arxiv.org/abs/1911.00003).
- [7] M. Aidelsburger, L. Barbiero, A. Bermudez, T. Chanda, A. Dauphin, D. González-Cuadra, P. R. Grzybowski, S. Hands, F. Jendrzejewski, J. Jünemann, G. Juzeliūnas, V. Kasper, A. Piga, S.-J. Ran, M. Rizzi, G. Sierra, L. Tagliacozzo, E. Tirrito, T. V. Zache, J. Zakrzewski, E. Zohar, and M. Lewenstein, Cold atoms meet lattice gauge theory, *Phil. Trans. R. Soc. A* **380**, 20210064 (2021), [arXiv:2106.03063](https://arxiv.org/abs/2106.03063).
- [8] I. Petrides, H. M. Price, and O. Zilberberg, Six-dimensional quantum Hall effect and three-dimensional topological pumps, *Phys. Rev. B* **98**, 125431 (2018), [arXiv:1804.01871](https://arxiv.org/abs/1804.01871).
- [9] C. H. Lee, Y. Wang, Y. Chen, and X. Zhang, Electromagnetic response of quantum Hall systems in dimensions five and six and beyond, *Phys. Rev. B* **98**, 094434 (2018), [arXiv:1803.07047](https://arxiv.org/abs/1803.07047).
- [10] H. M. Price, Four-dimensional topological lattices through connectivity, *Phys. Rev. B* **101**, 205141 (2020), [arXiv:1806.05263](https://arxiv.org/abs/1806.05263).
- [11] G. Žlabys, C.-h. Fan, E. Anisimovas, and K. Sacha, Six-dimensional time-space crystalline structures, *Phys. Rev. B* **103**, L100301 (2021), [arXiv:2012.02783](https://arxiv.org/abs/2012.02783).
- [12] Y.-Q. Zhu, Z. Zheng, G. Palumbo, and Z. D. Wang, Topological electromagnetic effects and higher second Chern numbers in four-dimensional gapped phases, *Phys. Rev. Lett.* **129**, 196602 (2022), [arXiv:2203.16153](https://arxiv.org/abs/2203.16153).
- [13] F. Wilczek, Quantum time crystals, *Phys. Rev. Lett.* **109**, 160401 (2012), [arXiv:1202.2539](https://arxiv.org/abs/1202.2539).
- [14] A. Shapere and F. Wilczek, Classical time crystals, *Phys. Rev. Lett.* **109**, 160402 (2012), [arXiv:1202.2537](https://arxiv.org/abs/1202.2537).
- [15] L. Guo, *Phase Space Crystals* (IOP Publishing, 2021).
- [16] K. Sacha, *Time Crystals* (Springer International Publishing, 2020).
- [17] K. Sacha and J. Zakrzewski, Time crystals: a review, *Rep. Prog. Phys.* **81**, 016401 (2018), [arXiv:1704.03735](https://arxiv.org/abs/1704.03735).
- [18] P. Hannaford and K. Sacha, Condensed matter physics in big discrete time crystals, *AAPPS Bulletin* **32**, 12 (2022), [arXiv:2202.05544](https://arxiv.org/abs/2202.05544).
- [19] T. Li, Z.-X. Gong, Z.-Q. Yin, H. T. Quan, X. Yin, P. Zhang, L.-M. Duan, and X. Zhang, Space-time crystals of trapped ions, *Phys. Rev. Lett.* **109**, 163001 (2012), [arXiv:1206.4772](https://arxiv.org/abs/1206.4772).
- [20] Q. Gao and Q. Niu, Floquet-Bloch oscillations and intraband Zener tunneling in an oblique spacetime crystal, *Phys. Rev. Lett.* **127**, 036401 (2021), [arXiv:2011.00421](https://arxiv.org/abs/2011.00421).
- [21] Y. Braver, C.-h. Fan, G. Žlabys, E. Anisimovas, and K. Sacha, Two-dimensional Thouless pumping in time-space crystalline structures, *Phys. Rev. B* **106**, 144301 (2022), [arXiv:2206.14804](https://arxiv.org/abs/2206.14804).
- [22] M. Łącki, M. A. Baranov, H. Pichler, and P. Zoller, Nanoscale “dark state” optical potentials for cold atoms, *Phys. Rev. Lett.* **117**, 233001 (2016), [arXiv:1607.07338](https://arxiv.org/abs/1607.07338).
- [23] J. Tangpanitanon, V. M. Bastidas, S. Al-Assam, P. Roushan, D. Jaksch, and D. G. Angelakis, Topological pumping of photons in nonlinear resonator arrays, *Phys. Rev. Lett.* **117**, 213603 (2016), [arXiv:1607.04050](https://arxiv.org/abs/1607.04050).
- [24] T. Haug, R. Dumke, L.-C. Kwek, and L. Amico, Topological pumping in Aharonov–Bohm rings, *Commun. Phys.* **2**, 10.1038/s42005-019-0229-2 (2019), [arXiv:1810.08525](https://arxiv.org/abs/1810.08525).
- [25] J. H. Shirley, Solution of the Schrödinger equation with a Hamiltonian periodic in time, *Phys. Rev.* **138**, B979 (1965).
- [26] A. Buchleitner, D. Delande, and J. Zakrzewski, Non-dispersive wave packets in periodically driven quantum systems, *Phys. Rep.* **368**, 409 (2002), [arXiv:quant-ph/0210033](https://arxiv.org/abs/quant-ph/0210033).
- [27] M. Holthaus, Floquet engineering with quasienergy bands of periodically driven optical lattices, *J. Phys. B: At., Mol. Opt. Phys.* **49**, 013001 (2015), [arXiv:1510.09042](https://arxiv.org/abs/1510.09042).
- [28] See Supplemental Material for details on diagonalization of the Floquet Hamiltonian, construction of the Wannier states, demonstration of pumping dynamics, and definition of the fourth Chern number.
- [29] C. Rackauckas and Q. Nie, DifferentialEquations.jl – a performant and feature-rich ecosystem for solving differential equations in Julia, *J. Open Res. Software* **5**, 15 (2017).
- [30] C. Rackauckas and Q. Nie, Confederated modular differential equation APIs for accelerated algorithm development and benchmarking, *Adv. Eng. Software* **132**, 1 (2019), [arXiv:1807.06430](https://arxiv.org/abs/1807.06430).
- [31] W. Kahan and R.-C. Li, Composition constants for raising the orders of unconventional schemes for ordinary differential equations, *Math. Comput.* **66**, 1089 (1997).
- [32] R. I. McLachlan and P. Atela, The accuracy of symplectic integrators, *Nonlinearity* **5**, 541 (1992).

- [33] P. K. Mogensen and A. N. Riseth, Optim: A mathematical optimization package for Julia, *J. Open Source Software* **3**, 615 (2018).
- [34] D. P. Sanders and L. Benet, *JuliaIntervals/IntervalArithmetic.jl: v0.20.8* (2022).
- [35] J. Bezanson, A. Edelman, S. Karpinski, and V. B. Shah, Julia: A fresh approach to numerical computing, *SIAM Rev.* **59**, 65 (2017), [arXiv:1411.1607](https://arxiv.org/abs/1411.1607).
- [36] See <https://github.com/yakovbraver/TTSC.jl> for the package source code.
- [37] A. A. Aligia and G. Ortiz, Quantum mechanical position operator and localization in extended systems, *Phys. Rev. Lett.* **82**, 2560 (1999), [arXiv:cond-mat/9810348](https://arxiv.org/abs/cond-mat/9810348).
- [38] J. Asbóth, L. Oroszlány, and A. Pályi, *A Short Course on Topological Insulators*, Lecture Notes in Physics, Vol. 919 (Springer International Publishing, 2016) [arXiv:1509.02295](https://arxiv.org/abs/1509.02295).
- [39] D. Xiao, M.-C. Chang, and Q. Niu, Berry phase effects on electronic properties, *Rev. Mod. Phys.* **82**, 1959 (2010), [arXiv:0907.2021](https://arxiv.org/abs/0907.2021).
- [40] S. Nakajima, T. Tomita, S. Taie, T. Ichinose, H. Ozawa, L. Wang, M. Troyer, and Y. Takahashi, Topological Thouless pumping of ultracold fermions, *Nat. Phys.* **12**, 296 (2016), [arXiv:1507.02223](https://arxiv.org/abs/1507.02223).
- [41] M. Lohse, C. Schweizer, O. Zilberberg, M. Aidelsburger, and I. Bloch, A Thouless quantum pump with ultracold bosonic atoms in an optical superlattice, *Nat. Phys.* **12**, 350 (2016), [arXiv:1507.02225](https://arxiv.org/abs/1507.02225).

Supplementary Material for: Eight-dimensional topological systems simulated using time-space crystalline structures

Yakov Braver,¹ Egidijus Anisimovas,¹ and Krzysztof Sacha²

¹*Institute of Theoretical Physics and Astronomy,
Vilnius University, Saulėtekio 3, LT-10257 Vilnius, Lithuania*
²*Instytut Fizyki Teoretycznej, Uniwersytet Jagielloński,
ulica Profesora Stanisława Łojasiewicza 11, PL-30-348 Kraków, Poland*

I. DIAGONALIZATION OF FLOQUET HAMILTONIAN

In this section, we sketch the diagonalization of the Floquet Hamiltonian

$$\hat{\mathcal{H}}_k = \hat{H}_k - i\partial_t. \quad (\text{S1})$$

Here, we have introduced the quasimomentum index, stemming from the spatial part of the problem. Specifically, we have

$$\hat{H}_k(x, t|\varphi_t) = \hat{h}_k(x) + \xi_S(x, t) + \xi_L(x, t|\varphi_t) \quad (\text{S2})$$

where

$$\hat{h}_k = (\hat{p}_x + k)^2 + V \sum_{n=0}^{3N} \delta(x - \frac{na}{3}) + U \sum_{n=0}^2 g_n(x) \cos(\varphi_x + \frac{2\pi n}{3}) \quad (\text{S3})$$

with

$$g_n(x) = \begin{cases} 1, & \frac{n}{3}a \leq x \bmod a < \frac{n+1}{3}a, \\ 0, & \text{otherwise,} \end{cases} \quad (\text{S4})$$

and

$$\xi_S(x, t) = \lambda_S \cos(\frac{12\pi x}{a}) \cos(2\omega t), \quad (\text{S5a})$$

$$\xi_L(x, t|\varphi_t) = \lambda_L \cos(\frac{6\pi x}{a}) \cos(\omega t + \varphi_t). \quad (\text{S5b})$$

It is a standard exercise to obtain the Bloch modes $\psi_{m,k}$ and eigenenergies $E_{m,k}$ for a delta-function Hamiltonian (S3). The next step is to solve the eigenvalue problem

$$\hat{\mathcal{H}}_k v_{n,k}(x, t) = \varepsilon_{n,k} v_{n,k}(x, t). \quad (\text{S6})$$

Instead of the full diagonalization of the Floquet Hamiltonian $\hat{\mathcal{H}}_k$, our aim is to obtain an effective (secular) time-independent Hamiltonian which can be more easily diagonalized. To this end we perform a time-dependent unitary transformation

$$\psi'_{m,k}(x, t) = e^{-i\nu(m)\omega t/s} \psi_{m,k}(x). \quad (\text{S7})$$

Here, the function $\nu(m) = \lceil m/3 \rceil$ (where $\lceil \dots \rceil$ is the ceiling operation) transforms the level numbers $m = 1, 2, 3, 4, 5, 6, \dots$ into band indices

$$\nu = 1, 1, 1, 2, 2, 2, 3, 3, 3, \dots \quad (\text{S8})$$

Note that this labeling is correct as long as we keep U small enough so that the difference of depths of the sites is always smaller than the gaps between the energy bands of the unperturbed Hamiltonian.

The diagonal matrix elements of $\hat{\mathcal{H}}_k$ are

$$\langle \psi'_{m',k} | \left(\hat{h}_k - i\frac{\partial}{\partial t} \right) | \psi'_{m,k} \rangle = \left(E_{m,k} - \frac{\nu(m)\omega}{s} \right) \delta_{m',m}. \quad (\text{S9})$$

For the perturbation term ξ_L , we obtain

$$\begin{aligned} \langle \psi'_{m',k} | \xi_L | \psi'_{m,k} \rangle &= \lambda_L \cos(\omega t + \varphi_t) e^{-i(\omega/s)[\nu(m)-\nu(m')]t} \\ &\quad \times \int_0^a dx \psi_{m',k}^*(x) \cos(\frac{6\pi x}{a}) \psi_{m,k}(x). \end{aligned} \quad (\text{S10})$$

Applying the secular approximation, we replace

$$\cos(\omega t + \varphi_t) e^{-i(\omega/s)[\nu(m)-\nu(m')]t} \quad (\text{S11})$$

with its time-independent contribution

$$\frac{1}{2} (e^{i\varphi_t} \delta_{\nu'+s,\nu} + e^{-i\varphi_t} \delta_{\nu'-s,\nu}), \quad (\text{S12})$$

where $\nu' \equiv \nu(m')$. Similarly, we have

$$\begin{aligned} \langle \psi'_{m',k} | \xi_S | \psi'_{m,k} \rangle &= \lambda_S \cos(2\omega t) e^{-i(\omega/s)[\nu(m)-\nu(m')]t} \\ &\quad \times \int_0^a dx \psi_{m',k}^*(x) \cos(\frac{12\pi x}{a}) \psi_{m,k}(x). \end{aligned} \quad (\text{S13})$$

where we replace

$$\cos(2\omega t) e^{-i(\omega/s)[\nu(m)-\nu(m')]t} \quad (\text{S14})$$

with

$$\frac{1}{2} (\delta_{\nu'+2s,\nu} + \delta_{\nu'-2s,\nu}), \quad (\text{S15})$$

Figure S1(a) displays schematically the coupling of the eigenenergy bands of \hat{h}_k induced by the perturbations. Each band of \hat{h}_k consists of three subbands because each cell of the spatial potential of \hat{h}_k contains three sites, but this is not detailed in the figure. As a result of the secular approximation, each level of the ν th band is coupled to all the levels of bands $\nu \pm s$ (via ξ_L) and $\nu \pm 2s$ (via ξ_S); in our case, $s = 2$. The driving frequency is chosen as $\omega = \Omega s$ with Ω being the energy gap between certain bands μ and $\mu + 1$. In practice, however, we fine-tune ω_μ to get the optimal quasienergy spectrum. Below, we will assume the working point of $\mu = 30$, which yields $E_{31} - E_{30} \approx 340$ for $a = 4$. This is consistent with the result calculated for the problem of a particle in an infinitely deep potential well of width $l = a/3$: in recoil units, the energy spectrum is $E_\nu = (\nu\pi/l)^2$. This also allows one to estimate the frequency: $\Omega = E_{\mu+1} - E_\mu = (2\mu + 1)\frac{\pi^2}{l^2}$. In a small neighborhood of the μ th energy band, the spectrum is close to being equidistant, therefore, transitions such as $E_{\mu-1} \leftrightarrow E_{\mu+1}$ and $E_{\mu+1} \leftrightarrow E_{\mu+3}$ are almost resonant with the frequency ω .

A sketch of the quasienergy spectrum of $\hat{\mathcal{H}}_k$ is given in Fig. S1(b). The bands of \hat{h}_k become grouped into overlapping pairs, and the resonant bands are the lowest. This can be seen by employing the above estimates of the energy spectrum E_ν and the resonant frequency Ω . Suppressing the k index, we find from Eq. (S9) that

$$\mathcal{H}_{\mu+\beta, \mu+\beta} = E_{\mu+\beta} - \Omega(\mu+\beta) = \mathcal{H}_{\mu, \mu} + (\beta^2 - \beta)\frac{\pi^2}{l^2}, \quad (\text{S16})$$

where integer (band) index β runs from $1 - \mu$ to infinity. Assuming the perturbation is small, the above expression yields the Floquet quasienergy spectrum shown in Fig. S1(b). The lowest are the levels μ and $\mu + 1$, whose energies should coincide according to Eq. (S16).

The actual quasienergy spectrum is shown in Fig. S2(a) for the case of simultaneous time-space pumping ($\varphi_x = \varphi_t$), with only the resonant bands displayed. These correspond precisely to the bands $\mu - 1$ through $\mu + 2$ shown schematically in Fig. S1(b).

Returning to the problem of finding the eigenfunctions of $\hat{\mathcal{H}}_k$, it remains to numerically diagonalize the obtained matrix for each k to find the coefficients $b_{m,k}^{(n)}$ of the expansion

$$v_{n,k}(x, t) = \sum_{m=1}^{\infty} b_{m,k}^{(n)} \psi'_{m,k}(x, t). \quad (\text{S17})$$

All calculations have been performed using a number of software packages [1–6] written in the Julia programming language [7]. The source code of our package is available on GitHub [8].

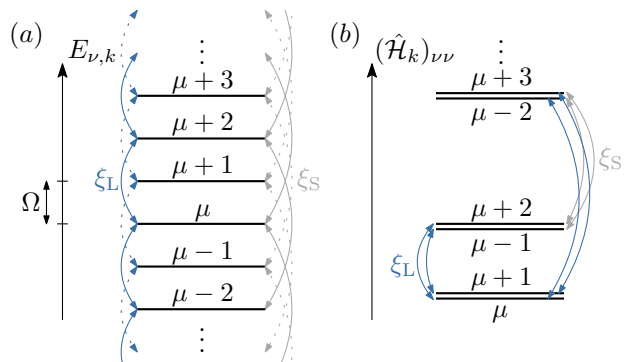


Figure S1. Schematic representation of the perturbation-induced band coupling (distances between bands not drawn to scale). (a) Eigenenergy bands of the unperturbed Hamiltonian \hat{h}_k in the vicinity of a certain resonant band whose number is μ . Each horizontal line represents an energy band (which contains three subbands) (b) Diagonal elements of Floquet Hamiltonian represented as coupled quasienergy levels. Only the couplings that have the most effect are shown.

II. VISUALIZATION OF TIME-SPACE PUMPING USING THE WANNIER FUNCTIONS

To analyze the pumping dynamics, we construct Wannier functions $w_\ell(x, t)$ by diagonalizing the periodic position operator $e^{i\frac{2\pi}{Na}x}$ [9, 10]. The calculation is performed in the basis of functions $u_{n,k}(x, t) = e^{ikx}v_{n,k}(x, t)$, where we have complemented the Floquet–Bloch modes $v_{n,k}$ by the exponential factor to obtain the “full” wave function defined on $x \in [0; Na)$. Diagonalization yields the coefficients $d_{n,k}^{(\ell)}$ of the expansion

$$w_\ell(x, t) = \sum_{n,k} d_{n,k}^{(\ell)} u_{n,k}(x, t). \quad (\text{S18})$$

Diagonalization has to be performed at a single fixed time moment at which the modes $u_{n,k}$ do not overlap strongly so that the resulting Wannier functions exhibit the required temporal localization [11]. In the relevant cases we sum over all quasimomenta k , while index n runs over a selected range of modes. Figure S2(b) displays the functions w_ℓ at $\varphi_x = \varphi_t = 0$ constructed by mixing the four modes corresponding to the highest band in the spectrum in Fig. S2(a) (highlighted in orange). The resulting functions inherit the spatial localization of the Floquet–Bloch modes being mixed and, consequently, are confined to a single spatial site. A detector placed at one of the turning points of any spatial site will be registering periodic arrival of a particle, and it is precisely this periodicity that allows us to speak of a crystalline structure in time [11–13]. The shaded regions in Fig. S2(b) indicate the parts of the time-space that we associate — by convention — with the four temporal sites: sites $\alpha = 1, 2$ (green and red) belong to the first temporal cell, while $\alpha = 3, 4$ (beige and blue) belong to the second. For example, a

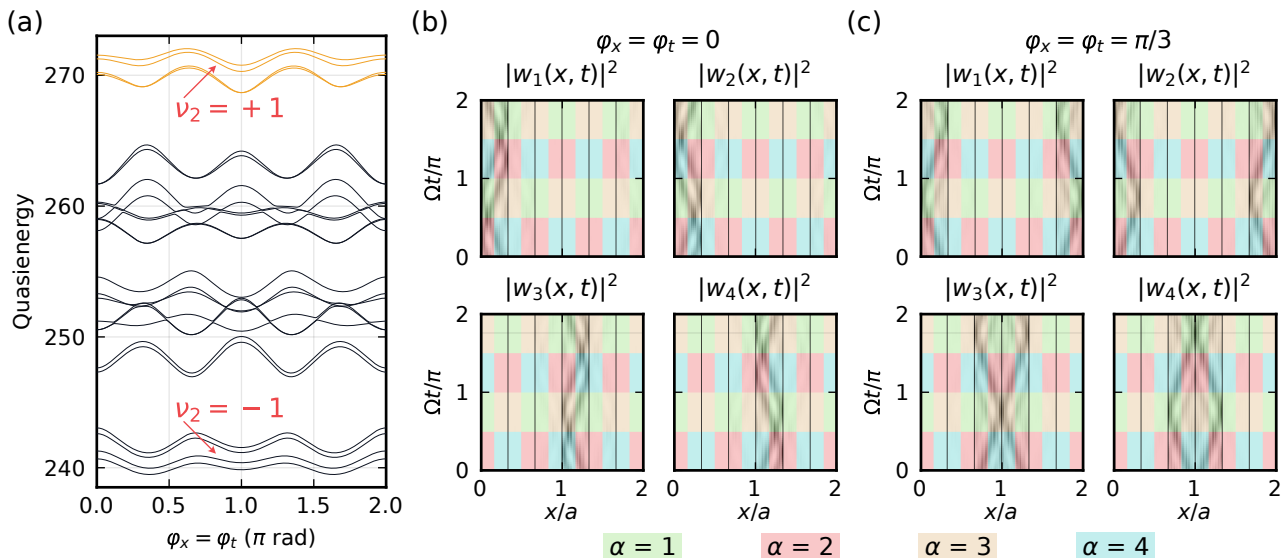


Figure S2. Time-space adiabatic pumping in a 2D time-space crystal with $s = 2$ temporal cells and $N = 2$ spatial cells that consists of three spatial sites. The following values of parameters were used: $a = 4.000$, $V = 2000$, $U = 7.000$, $\omega = 676.8$, $\lambda_S = 10.00$, $\lambda_L = 20.00$. (a) Quasienergy spectrum of the Floquet Hamiltonian $\hat{\mathcal{H}}$. (b) The Wannier functions $|w_\ell(x, t)|^2$ at $\varphi_x = \varphi_t = 0$, represented by black regions. The shaded areas indicate the extent of the temporal sites numbered by α : sites $\alpha = 1, 2$ belong to the first temporal cell, while $\alpha = 3, 4$ belong to the second. Black vertical lines separate the spatial sites. (c) Same as (b) at $\varphi_x = \varphi_t = \pi/3$.

particle in the state w_1 will be passing a detector placed at $x = 0$ at time intervals $(\Omega t \bmod 2\pi) \in [0, \pi]$, meaning that it occupies the first temporal cell. In the course of the pumping, the states transition both in the spatial and in the temporal directions. At $\varphi_x = \varphi_t = \pi/3$ [see Fig. S2(c)], the states are localized in a single temporal site while occupying two neighboring spatial sites. At the end of the pumping cycle, states w_1 and w_4 effectively exchange their initial occupations, as do states w_2 and w_3 (not shown). Thus, having divided the time-space into temporal and spatial cells as shown in the figure, we find that at the end of a time-space pumping cycle each Wannier function occupies spatial and temporal cells different from the starting ones.

III. THE WANNIER BASIS AND THE TIGHT-BINDING PICTURE

To switch to the tight-binding description, we construct the Wannier basis functions by mixing the states corresponding to all the resonant levels of the Floquet quasienergy spectrum, i.e., all levels shown in Fig. S2(a). In practice, two out of four Wannier functions localized in a single spatial site come out not well-localized in the temporal dimensions. To alleviate this issue, we perform an additional unitary transformation of the two problematic Wannier functions w_a and w_b :

$$\begin{pmatrix} \tilde{w}_a \\ \tilde{w}_b \end{pmatrix} = \hat{U}(\gamma, \theta, \phi) \begin{pmatrix} w_a \\ w_b \end{pmatrix}. \quad (\text{S19})$$

Here, $\hat{U}(\gamma, \theta, \phi)$ is a general 2×2 unitary matrix

$$\hat{U}(\gamma, \theta, \phi) = e^{i\gamma \mathbf{n}(\theta, \phi) \cdot \boldsymbol{\sigma}} \quad (\text{S20})$$

where $\gamma \in [0, 2\pi]$, $\boldsymbol{\sigma}$ is a vector of Pauli matrices, and \mathbf{n} is a three-component unit vector parameterized by an azimuthal angle $\phi \in [0, 2\pi]$ and a polar angle $\theta \in [0, \pi]$. We optimize the angles γ , θ , and ϕ to get the least possible overlap of probability densities of \tilde{w}_a and \tilde{w}_b . Specifically,

$$\iint dx dt \left| |\tilde{w}_3|^2 - |\tilde{w}_2|^2 \right| \rightarrow \max. \quad (\text{S21})$$

In what follows, the Wannier functions being discussed are the “optimized” ones.

In the studied case, we obtain $3N \times 2s = 24$ Wannier functions, which we are free to number as we see fit. Figure S3 shows, as an example, twelve Wannier functions localized in the first, second, and sixth spatial sites. As we can see, each of them is strongly localized in a single spatial and temporal site. The numbering convention is such that the ℓ th Wannier is localized in the j th spatial and the α th temporal sites, with $\ell = 2s(j-1) + \alpha$, where $j \in [1, 3N]$ and $\alpha \in [1, 2s]$. Note, however, that the temporal sites are assigned differently in the odd and even spatial sites. For example, a particle is said to occupy the first temporal site (green areas in Fig. S3) of an *odd* spatial site if it will most likely be found at the *right* turning point in the interval $(\Omega t \bmod 2\pi) \in [3\pi/2, 2\pi]$, see w_1 in Fig. S3. On the other hand, a particle occupying the first temporal site of an *even* spatial site will most likely be

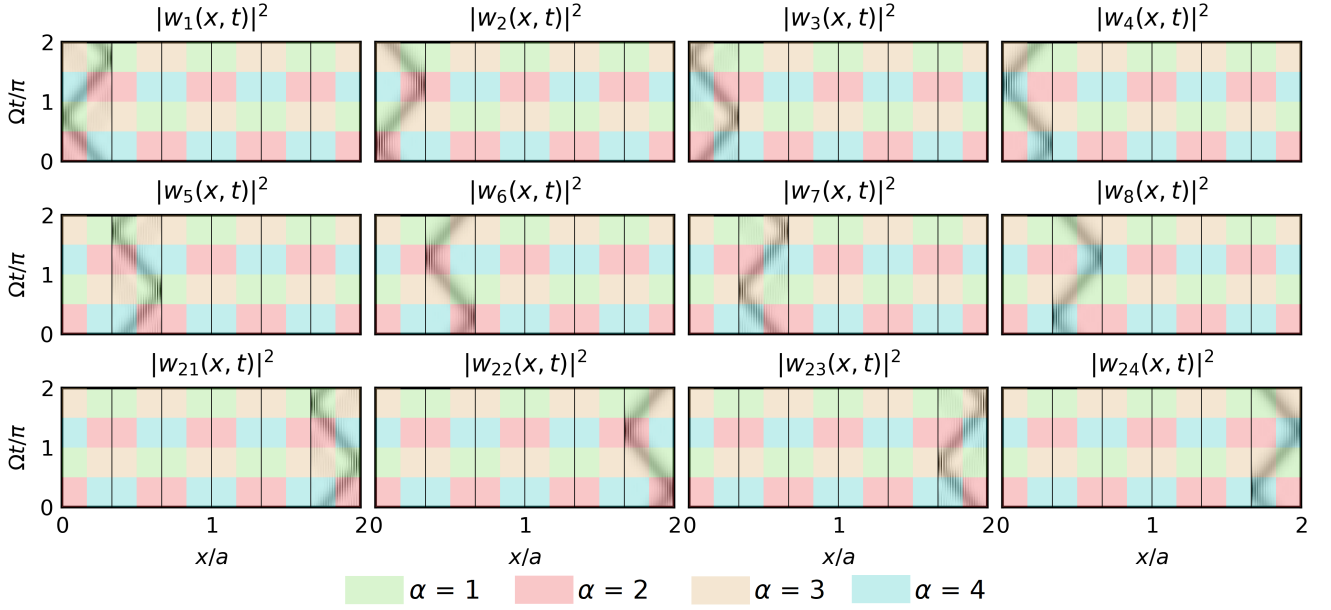


Figure S3. Twelve Wannier functions.

found found at the *left* turning point in the same interval $(\Omega t \bmod 2\pi) \in [3\pi/2, 2\pi]$, see w_5 in Fig. S3. Such a convention ensures the correct interpretation of the outcome of a pumping cycle, as demonstrated in Section II. Moreover, it allows one to obtain a tight-binding Hamiltonian

$$\hat{\mathcal{H}}_{\text{TB}}(\varphi_x, \varphi_t) = \sum_{\ell', \ell} J_{\ell'\ell}(\varphi_x, \varphi_t) \hat{a}_{\ell'}^\dagger \hat{a}_\ell \quad (\text{S22})$$

that can be decomposed into two independent parts — the spatial Hamiltonian and the temporal one. The absolute values of the matrix elements of $\hat{\mathcal{H}}_{\text{TB}}$ calculated at $\varphi_x = \varphi_t = 0$ are presented in Fig. S4, where the diagonal elements have been set to zero for visual clarity. It is apparent that the resulting matrix allows for the decomposition

$$\hat{\mathcal{H}}_{\text{TB}} \approx \hat{I}_x \otimes \hat{H}_t + \hat{H}_x \otimes \hat{I}_t \equiv \hat{\mathcal{H}}'_{\text{TB}}, \quad (\text{S23})$$

as discussed in the Letter. In our case, we take \hat{H}_t to be given by the top left 4×4 block of $\hat{\mathcal{H}}'_{\text{TB}}$, while \hat{H}_x is given by

$$\hat{H}_x = \begin{pmatrix} J_{11} & |J_{15}| & 0 & 0 & 0 & |J_{15}| \\ |J_{15}| & J_{55} & |J_{15}| & 0 & 0 & 0 \\ 0 & |J_{15}| & J_{99} & |J_{15}| & 0 & 0 \\ 0 & 0 & |J_{15}| & J_{11} & |J_{15}| & 0 \\ 0 & 0 & 0 & |J_{15}| & J_{55} & |J_{15}| \\ |J_{15}| & 0 & 0 & 0 & |J_{15}| & J_{99} \end{pmatrix}. \quad (\text{S24})$$

For simplicity, we assume that the phases of the the tunneling strengths have been eliminated by redefining the global phases of the basis functions. The crudest part of the separability approximation (S23) is the dropping of the off-diagonal elements in the blue blocks (and their conjugate counterparts) highlighted in Fig. S4.

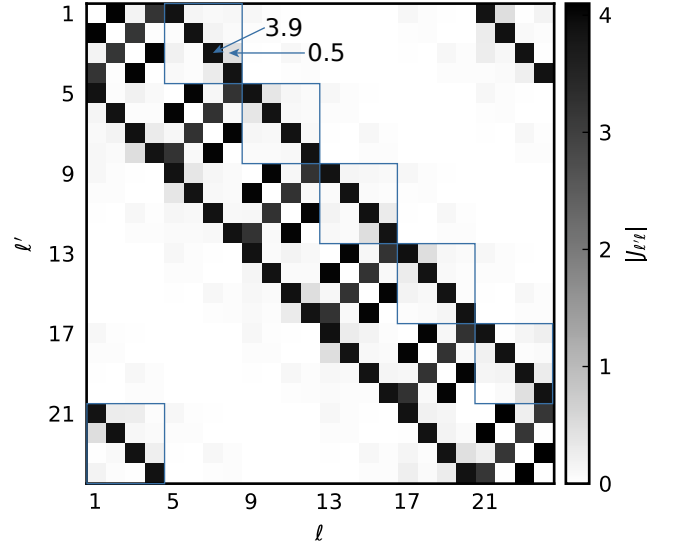


Figure S4. Absolute values $|J_{\ell'\ell}|$ of the matrix elements of $\hat{\mathcal{H}}_{\text{TB}}$ at $\varphi_x = \varphi_t = 0$. Diagonal elements have been set to zero for visual clarity. Values of J_{37} and J_{38} are explicitly indicated. The structure of the blue blocks is similar to the displayed one for all values of the phases φ_x and φ_t .

To extract the first Chern numbers ν_1 of the bands of Hamiltonians \hat{H}_x and \hat{H}_t , we may calculate the pumping dynamics. To this end, we consider the periodic coordinate operator, whose elements, in coordinate representation, are given by $X_{mm} = e^{i\frac{2\pi}{M}m}$, where $m \in [0, M-1]$ and M is the size of the Hamiltonian under consideration ($M = 6$ for \hat{H}_x and $M = 4$ for \hat{H}_t). Then, we diagonalize this operator in the subspace of the eigenstates of \hat{H}_x

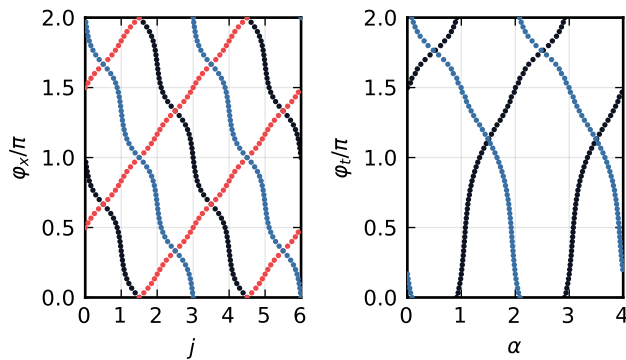


Figure S5. Dynamics of the Wannier centers. (a) Spatial pumping dynamics calculated based on \hat{H}_x . Black, red, and blue points represent, respectively, the positions of the Wannier centers calculated by mixing the eigenstates corresponding to the bottom, middle, and top bands in the spectrum of \hat{H}_x [see Fig. 2(a) in the Letter]. (b) Temporal pumping dynamics calculated based on \hat{H}_t . Black and blue points represent, respectively, the positions of the Wannier centers calculated by mixing the eigenstates corresponding to the bottom and top bands in the spectrum of \hat{H}_t [see Fig. 2(b) in the Letter].

or \hat{H}_t corresponding to a single band of the energy spectrum. The resulting eigenfunctions of \hat{X} are the Wannier functions, while the phases of the eigenvalues (scaled by $2\pi/M$) are their well-defined positions (also called the Wannier centers) [9, 10]. Black points in Fig. S5(a) show the dynamics of the Wannier centers obtained by considering the subspace of the lowest energy band of \hat{H}_x . It is apparent that the states are transferred by one cell (three sites) “to the left” during one pumping cycle. Blue points show an analogous result for the states of the highest energy band of \hat{H}_x , while the red points indicate a displacement by two cells per cycle in the opposite direction. The first Chern numbers of the bands are thus -1 , $+2$, and -1 for the bottom, middle, and the top energy bands of \hat{H}_x .

The temporal pumping based on \hat{H}_t is studied in Fig. S5(b). The black points indicate a displacement by a single cell “to the right” per pumping cycle taking place in the bottom energy band ($\nu_1 = +1$), while the blue points show a displacement by a single cell in the opposite direction for the top energy band ($\nu_1 = -1$).

IV. THE FOURTH CHERN NUMBER

As discussed in the Letter, combining two 4D systems described by $\hat{\mathcal{H}}_{\text{TB}}$ and constructed in orthogonal spatial dimensions yields an 8D system according to

$$\hat{\mathcal{H}}_{\text{8D}} = \hat{I} \otimes \hat{\mathcal{H}}_{\text{TB}}^{(x)} + \hat{\mathcal{H}}_{\text{TB}}^{(y)} \otimes \hat{I}. \quad (\text{S25})$$

The parameters of $\hat{\mathcal{H}}_{\text{8D}}$ are the components of the following formal vector:

$$\mathbf{R} = (k_x, \varphi_x, k_{t_x}, \varphi_{t_x}, k_y, \varphi_y, k_{t_y}, \varphi_{t_y}). \quad (\text{S26})$$

The Abelian Berry curvature is introduced using the eigenstates of a nondegenerate energy band of $\hat{\mathcal{H}}_{\text{8D}}$ as

$$\Omega_{\mu\nu}(\mathbf{R}) = -2\Im \langle \partial_\mu \zeta_{n,\mathbf{k}} | \partial_\nu \zeta_{n,\mathbf{k}} \rangle \quad (\text{S27})$$

where $\partial_\mu \equiv \frac{\partial}{\partial R^\mu}$, index μ runs from 1 through 8, $\mathbf{k} = (k_x, k_y, k_{t_x}, k_{t_y})$, and $|\zeta_{n,\mathbf{k}}\rangle$ is the cell-periodic part of the n th band eigenstate of $\hat{\mathcal{H}}_{\text{8D}}$. Let $|n, k_x, k_{t_x}\rangle$ be the cell-periodic part of the n th band eigenstate of $\hat{\mathcal{H}}_{\text{TB}}^{(x)}$; then (S25) implies $|\zeta_{n,\mathbf{k}}\rangle = |n, k_x, k_{t_x}\rangle \otimes |n, k_y, k_{t_y}\rangle$.

The fourth Chern number is given by [14]

$$\nu_4 = \frac{1}{(2\pi)^4} \int d^8 R \frac{\epsilon_{\mu_1, \dots, \mu_8}}{(2^4 \times 4!)} \Omega_{\mu_1 \mu_2} \Omega_{\mu_3 \mu_4} \Omega_{\mu_5 \mu_6} \Omega_{\mu_7 \mu_8}, \quad (\text{S28})$$

where $\epsilon_{\mu_1, \dots, \mu_8}$ is the totally antisymmetric tensor of rank 8. Due to the separability of the system, this expression simplifies to

$$\nu_4 = \frac{1}{(2\pi)^4} \int d^8 R \Omega_{12} \Omega_{34} \Omega_{56} \Omega_{78} = \nu_2^{(x, t_x)} \nu_2^{(y, t_y)}. \quad (\text{S29})$$

-
- [1] C. Rackauckas and Q. Nie, *J. Open Res. Software* **5**, 15 (2017).
 - [2] C. Rackauckas and Q. Nie, *Adv. Eng. Software* **132**, 1 (2019), arXiv:1807.06430.
 - [3] W. Kahan and R.-C. Li, *Math. Comput.* **66**, 1089 (1997).
 - [4] R. I. McLachlan and P. Atela, *Nonlinearity* **5**, 541 (1992).
 - [5] P. K. Mogensen and A. N. Riseth, *J. Open Source Software* **3**, 615 (2018).
 - [6] D. P. Sanders and L. Benet, “JuliaIntervals/IntervalArithmetic.jl: v0.20.8,” (2022).
 - [7] J. Bezanson, A. Edelman, S. Karpinski, and V. B. Shah, *SIAM Rev.* **59**, 65 (2017), arXiv:1411.1607.
 - [8] See <https://github.com/yakovbraver/TTSC.jl> for the package source code.
 - [9] J. Asbóth, L. Oroszlány, and A. Pályi, *A Short Course on Topological Insulators*, Lecture Notes in Physics, Vol. 919 (Springer International Publishing, 2016) arXiv:1509.02295.
 - [10] A. A. Aligia and G. Ortiz, *Phys. Rev. Lett.* **82**, 2560 (1999), arXiv:cond-mat/9810348.
 - [11] G. Žlabys, C.-h. Fan, E. Anisimovas, and K. Sacha, *Phys. Rev. B* **103**, L100301 (2021), arXiv:2012.02783.
 - [12] K. Sacha, *Time Crystals* (Springer International Publishing, 2020).
 - [13] Y. Braver, C.-h. Fan, G. Žlabys, E. Anisimovas, and K. Sacha, *Phys. Rev. B* **106**, 144301 (2022), arXiv:2206.14804.
 - [14] I. Petrides, H. M. Price, and O. Zilberberg, *Phys. Rev. B* **98**, 125431 (2018), arXiv:1804.01871.